

Large circular photogalvanic effect in non-centrosymmetric magnetic Weyl semimetal CeAlSi

Abhirup Roy Karmakar,^{1,*} A. Taraphder,^{1,†} and G. P. Das^{2,‡}

¹*Department of Physics, Indian Institute of Technology Kharagpur, W.B. 721302, India*

²*Research Institute for Sustainable Energy (RISE), TCG Centres for Research and Education in Science and Technology, Sector V, Salt Lake, Kolkata 700091, India*

(Dated: August 28, 2023)

The recent discovery of the Weyl semimetal CeAlSi with simultaneous breaking of inversion and time-reversal symmetries has opened up new avenues for research into the interaction between light and topologically protected bands. In this work, we present a comprehensive examination of shift current and injection current responsible for the circular photogalvanic effect in CeAlSi using first-principles calculations. Our investigation identifies a significant injection current of 1.2 mA/V^2 over a broad range in the near-infrared region of the electromagnetic spectrum, exceeding previously reported findings. In addition, we explored several externally controllable parameters to further enhance the photocurrent. A substantial boost in the injection current is observed when applying uniaxial strain along the c -axis of the crystal – a 5% strain results in a remarkable 64% increment. The exceptional photocurrent response in CeAlSi suggests that magnetic non-centrosymmetric Weyl semimetals may provide promising opportunities for novel photogalvanic applications.

Introduction. — Weyl semimetals have captivated the condensed matter physics community, drawing considerable attention due to their distinct electronic band structure and intriguing properties. These topological materials exhibit massless Weyl fermions as fundamental quasiparticles, in contrast to the conventional solid-state physics, and inspired cutting-edge research [1–3]. The unique characteristics of Weyl semimetals (WSM) are closely linked to their symmetry-related features, making them a fascinating subject of study. In particular, Weyl semimetals break two critical symmetries in the crystal lattice: time-reversal symmetry (TRS) and inversion symmetry (IS) [4]. Time-reversal symmetry ensures the equivalence of particle dynamics when played backward in time, while inversion symmetry relates the system’s behavior under spatial inversion. The breaking of these symmetries results in the formation of pairs of Weyl points in the electronic band structure. These Weyl points act as sources and sinks of quantized Berry curvature in momentum space [5]. Additionally, the breaking of TRS in Weyl semimetals [6–8] leads to the chiral anomaly — an astounding phenomenon resulting in an imbalance of chiral fermions in the presence of parallel electric and magnetic fields. This effect gives rise to exotic transport properties such as the negative longitudinal magnetoresistance [9–11] anomalous Hall effect [12–14], anomalous thermal Hall effect [15–17], anomalous Nernst effect [16–18] etc. The other class of WSMs with broken inversion symmetry [19–22] produce another set of interesting electronic and optical phenomena like nonlinear anomalous Hall effect [23–25], second harmonic generation [26–28], bulk photovoltaic effect [29–31], circular photogalvanic effect [32–34] etc.

Among the remarkable manifestations in Weyl semimetals, the nonlinear optical properties like bulk photovoltaic effect (BPVE) and circular photogalvanic effect (CPGE) have sparked a surge of interest and hold great promise for advancing the frontier of modern optoelectronics and photonics. The

bulk photovoltaic effect manifests as a nonlinear, optically-induced charge separation within the material’s bulk, arising from the breaking of inversion symmetry. This intriguing phenomenon suggests the tantalizing potential for harnessing sunlight and transforming it into electricity in an unconventional and efficient manner [35, 36]. As we delve into the mechanisms of this effect, we uncover a treasure trove of possibilities for a sustainable and greener future. Furthermore, the

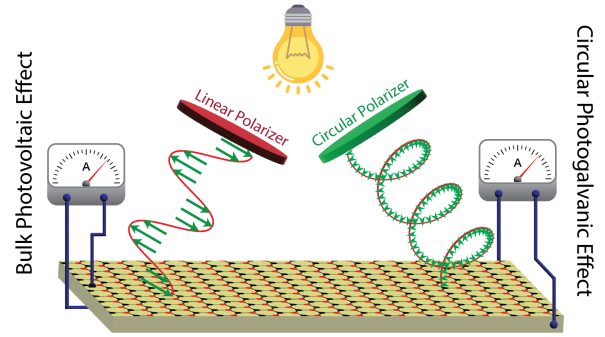


FIG. 1. **Schematic diagram:** The left and right parts of the figure demonstrate the bulk photovoltaic effect and the circular photogalvanic effect respectively.

circular photogalvanic effect, an engrossing manifestation of optoelectronic response unique to Weyl semimetals, unravels a dance between circularly polarized light and the chiral fermions [37–39]. This effect induces a photoinduced current resonating with the helicity of light, unlocking opportunities for innovative photonic devices and novel light manipulation techniques. It beckons us to venture into a new frontier of photonic technologies, where the collaboration of light and topological materials leads to a novel era of light-matter interactions.

To date, an array of Weyl semimetallic materials has been explored under both the symmetry classes, through experimental investigations as well as theoretical analyzes. Nonetheless, the pool of systems wherein both inversion and time-reversal symmetries are concurrently broken remains

* abhirup.phy@iitkgp.ac.in

† arghya@phy.iitkgp.ac.in

‡ gour.das@tcgcrest.org

limited. Notably, CeAlSi emerges as a candidate of this category, boasting noncollinear ferromagnetic order [40]. While considerable research has been devoted to studying its anomalous transport properties and Fermi arcs [40–44], the material presents numerous uncharted areas of paramount interest. In this work on CeAlSi, we present a comprehensive first-principles investigation of the injection current, a key contributor to the circular photogalvanic effect, and compare it with the shift current, which drives the bulk photovoltaic effect. Remarkably, our findings indicate a substantial magnitude of the injection current ($\sim 1.24 \text{ mA/V}^2$), surpassing previously reported literature results [45–49]. Intriguingly, it emerges as the dominant mechanism within the near-infrared region of the electromagnetic spectrum. In contrast, the contribution of the shift current remains comparatively limited with respect to the injection current. Moreover, our inquiry extends towards identifying several externally tunable parameters that positively influence the circular photocurrent. Interestingly, we observe a significant boost in the photocurrent through the application of uniaxial strain along the c -axis of the crystal. This noteworthy revelation opens new avenues for the advancement of photovoltaic technologies and underscores the material’s potential in light-driven applications.

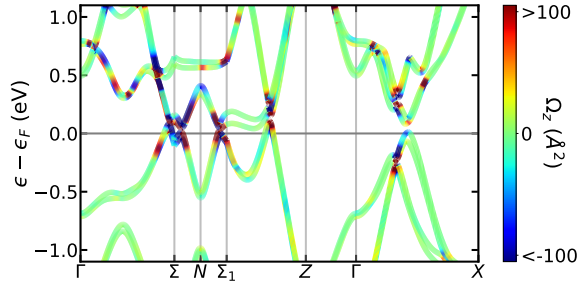


FIG. 2. Berry curvature resolved band structure along the high-symmetry path. The color coding represents the values of the z -component of Berry curvature as shown in the color bar.

Material information. — CeAlSi has a non-centrosymmetrically ordered structure with a space group of $I4_1md$ (No. 109) and is an isostructure of CeAlGe which was first proposed as a Ferromagnetic Weyl semimetal [50, 51]. Despite possessing a four-fold rotation axis (C_{4v}) and two vertical mirror planes (σ_v), the crystal structure lacks the horizontal mirror plane (σ_h) which is responsible for the breaking of inversion symmetry. We first performed the density functional theory (DFT) calculations with VASP [52] in a generalized gradient approximation (GGA) for exchange-correlation functional [53]. To account for the f -electrons of Ce atoms, an on-site Coulomb interaction of strength $U_{eff} = 7 \text{ eV}$ was added within the approach given by Dudarev *et al.* [54]. A tight-binding model with 52 bands was constructed using Wannier90 by feeding the Bloch wave functions obtained from DFT calculation [55, 56]. All other numerical calculations were performed in Python programming language and with the help of WannierBerri [57] package. The DFT calculation reveals that the system has a noncollinear Ferromagnetic order with net magnetization

vector [1.1, 1.1, 0.3]. The magnetization predominantly comes from the Ce- f orbitals alone with $0.89 \mu_B/\text{Ce}$ atom. The Berry curvature-resolved band structure with spin-orbit coupling (SOC) is plotted along the high-symmetry path $\Gamma - \Sigma - N - \Sigma_1 - Z - \Gamma - X$ (Fig. 2). The color coding is for z -component of the Berry curvature with values explained in the color bar outside. In the band structure, there are three crossings between the valence and conduction bands: two around the high-symmetry points Σ and one along the direction $N - \Sigma_1$. However, by scanning throughout the Brillouin zone in three-dimensional reciprocal space, we obtained 20 pairs of Weyl nodes with opposite chiralities in total. Next we discuss the theory and results of nonlinear photocurrents.

Nonlinear photocurrents. — Circular photogalvanic effect is the phenomenon where circularly polarized light incident on a material induces a time-dependent current density that manifests in a DC current response. Whereas, the bulk photovoltaic effect is a DC current response due to linearly polarized light. Although these two effects can be produced by various mechanisms, we focus here only on the second-order intrinsic contributions, namely the “shift current” and “injection current” for BPVE and CPGE, respectively. The total nonlinear photocurrent density in terms of the two can be written as,

$$\langle \mathbf{J}_{DC} \rangle^{(2)} = \langle \mathbf{J}_{SC} \rangle^{(2)} + \langle \mathbf{J}_{IC} \rangle^{(2)} \quad (1)$$

where,

$$\begin{aligned} \langle \mathbf{J}_{SC} \rangle^{(2)} &= \sigma_2^{abc}(0; \omega, -\omega) \mathbf{E}^b(\omega) \mathbf{E}^c(-\omega) \\ \frac{\langle \mathbf{J}_{IC} \rangle^{(2)}}{dt} &= \eta_2^{abc}(0; \omega, -\omega) \mathbf{E}^b(\omega) \mathbf{E}^c(-\omega) \end{aligned}$$

with a, b, c being the cartesian indices; σ_2^{abc} and η_2^{abc} are respectively the shift-current and injection current susceptibility tensor. The electric fields $\mathbf{E}(\omega)$ are real in case of linearly polarized light, whereas they are complex for circularly polarized light. The photocurrent tensors can be mathematically calculated using the following expressions [58]

$$\sigma_2^{abc} = -\frac{i\pi e^3}{2\hbar^2} \int \frac{d\mathbf{k}}{(2\pi)^3} \sum_{n,m} f_{nm} (r_{mn}^b r_{nm;a}^c + r_{mn}^c r_{nm;a}^b) \times \delta(\epsilon_{mn} - \hbar\omega) \quad (2)$$

$$\eta_2^{abc} = \frac{\pi e^3}{2\hbar^2} \int \frac{d\mathbf{k}}{(2\pi)^3} \sum_{n,m} \Delta_{mn}^a f_{nm} (r_{mn}^b r_{nm}^c - r_{mn}^c r_{nm}^b) \times \delta(\epsilon_{mn} - \hbar\omega) \quad (3)$$

where, m, n are the band indices. $\epsilon_{mn} = \epsilon_m - \epsilon_n$, $f_{mn} = f_m - f_n$ are the differences of band energies and Fermi-Dirac occupation number respectively. $\Delta_{mn}^a = \partial_{k_a} \epsilon_{mn}$, $r_{mn}^a = A_{mn}^a = i\langle m | \partial_{k_a} | n \rangle$ ($m \neq n$) is the interband matrix element (off-diagonal Berry connection), and $r_{nm;a}^b = \partial_{k_a} r_{mn}^b - i(A_{nn}^a - A_{mm}^a) r_{mn}^b$ is the generalized derivative of the matrix element. For numerical evaluation of Eq. (3), we replace delta

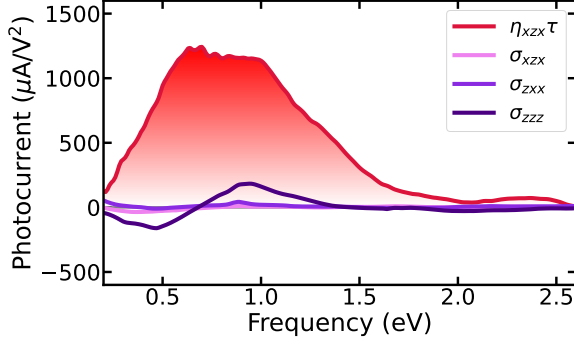


FIG. 3. Injection current and shift currents are plotted as a function of incident light frequency for $\frac{\hbar}{\tau} = 20$ meV. $\eta_{xzx}\tau$ has the maximum value of $1242 \mu\text{A}/\text{V}^2$ and is dominant throughout a broad region in the infrared spectrum with two peaks located at 0.64 and 0.99 eV. The intensity of the red gradients is proportional to the corresponding values. On the other hand, shift current values remain well below the above-mentioned value of injection current and have two peaks at 0.47 eV and 0.94 eV.

function with the Lorentzian function $\frac{1}{\pi} \frac{\Gamma}{(\epsilon_{mn} - \hbar\omega)^2 + \Gamma^2}$, where $\Gamma = \hbar/\tau$ (τ is the relaxation time).

For a two-band model system, the above equation takes the form [48] :

$$\eta_2^{abc} = \frac{i\pi e^3}{2\hbar^2} \int \frac{d\mathbf{k}}{(2\pi)^3} \Delta_{12}^a \Omega_v^{bc} \times \delta(\epsilon_{21} - \hbar\omega) \quad (4)$$

where 1,2 correspond to valence and conduction bands respectively, and Ω_v^{bc} is the valence band Berry curvature. Although, in this work we are dealing with a realistic material with 52 bands, it is important to understand from Eq. (3) that all the interband transitions counted are between two bands m and n . And hence, having non-zero values of Berry curvature for the bands will give us a hint towards getting a finite value injection current. Fig. 2 exhibits the finiteness of the curvature for each band near Fermi level along the high symmetry k-path.

For this particular crystal class, the non-zero susceptibility tensor elements are $xzx = yzy$, $xxz = yyz$, $zxx = zyy$ and zzz [59]. However, according to the equations (2), (3) and ref. [58], $\sigma_2^{xzx} = \sigma_2^{xxz}$, $\eta_2^{xzx} = -\eta_2^{xxz}$ and $\eta_2^{zxx} = \eta_2^{zzz} = 0$. So, the only independent non-zero elements are σ_2^{xzx} , σ_2^{xxz} , σ_2^{zxx} and η_2^{xzx} . The first index represents the direction of photocurrent and the last two represent the polarization of light. Hence, shift current is generated by both linearly-polarized (σ_2^{xzx} , σ_2^{zxx}) and circularly-polarized (σ_2^{xxz}) light, whereas injection current can only be produced by circularly-polarized light (η_2^{xzx}). Also, swapping the helicity of the incident light ($zx \leftrightarrow xz$), reverses the direction of the current, in accordance with the definition of CPGE.

Since, the photocurrent tensors are obtained from transitions between multiple bands (both real and virtual), they are heavily dependent on the incident light frequency. Also, the relaxation time (τ) plays a major role in the photocurrent calculation, especially for injection current. For a typical metallic system $\frac{\hbar}{\tau}$ should be of the order of $k_B T$. Here, we do our calculations in room temperature ($T = 300$ K) and accord-

ingly choose $\frac{\hbar}{\tau} = 20$ meV ($\tau \sim 33fs$). We integrate the quantities mentioned in the equations (2) and (3) throughout the Brillouin zone considering transitions between all the 52 bands. The independent injection current component (η_2^{xzx}) along with the non-zero shift current tensors are plotted in Fig. 3. It is quite interesting to see that η_2^{xzx} attains noticeably large values over a wide range in the electromagnetic spectrum with a maximum of $1242 \mu\text{A}/\text{V}^2$. This current is induced along the a -axis of the crystal when a right-circularly polarized light is irradiated along the b -axis. Flipping the helicity of the light reverses the sign of the current. The two visible peaks are situated at 0.64 and 0.99 eV which correspond to wavelengths of 1940 nm and 1250 nm respectively, falling in the near-infrared (NIR) region ($2526 - 780 \text{ nm}$). As per the full width at half maximum (FWHM), η_{xzx} turns out to be dominant in the range $0.39 - 1.29 \text{ eV}$ ($3180 - 961 \text{ nm}$). Although the current decreases sharply beyond 1 eV, the contribution is still finite in the visible light area with $175 \mu\text{A}/\text{V}^2$ at 1.63 eV (lower edge of the visible spectrum) and continues to decrease until 2.6 eV where the value becomes zero. On the other hand, shift current which is induced by the separation of charges, does not go as high as the injection current. The largest component σ_{zzz} attains a maximum current of $185 \mu\text{A}/\text{V}^2$ at 0.94 eV and has another negative peak of $-155 \mu\text{A}/\text{V}^2$ at 0.47 eV. It is produced along the c -axis of the crystal when a linearly polarized light with polarization along the same direction falls on the material. The other two components have negligible response though. In the following part of the paper, we do further analysis of η_{xzx} in presence of strain.

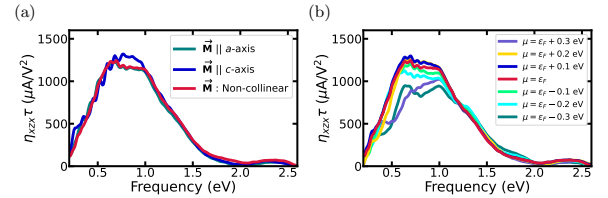


FIG. 4. (a) Injection current plotted for different orientations of magnetic order. The photocurrent profile for magnetization along a -axis (green) is almost similar to that of the noncollinear ground state (red). However, the plateau region gets lifted when magnetization is along c -axis (blue), consequently shifting the initial peak position. (b) Multiple η_{xzx} profiles plotted by varying chemical potential (μ). It shows that the peak value increases only for a slight increase (up to 0.2 eV) in chemical potential from ϵ_F . Increasing μ further or decreasing below ϵ_F lowers the value of η_{xzx} .

External influences. — Here, we look for the externally tunable parameters in order to maximize the current output. Motivated by the work of Alam *et al.* [41], we study CPGE for two different magnetic configurations. In its ground state, CeAlSi has noncollinear magnetic order with moments directed between a -axis and b -axis on ab -plane. We calculate injection current for two cases of collinear magnetization: (i) magnetic moments along a -axis and (ii) magnetic moments along c -axis and plot them in Fig. 4a. It turns out that when magnetization is along a -axis, peak of the photocurrent pro-

file remains almost similar to that of the ground state with noncollinear order. However, when the moments are forced to align towards the hard axis (c -axis), the peak value increases by a small amount. The peak now shifts to the center of the plateau region and all the values in that region get enhanced. To be quantitative, the peak goes from $1242 \mu\text{A}/\text{V}^2$ to $1320 \mu\text{A}/\text{V}^2$. To proceed with another approach, we change the chemical potential (μ) of the system and study the injection current profile, for multiple values of μ between -0.3 eV and $+0.3 \text{ eV}$ relative to the Fermi level (Fig. 4b). We observe that, when we increase the chemical potential above ϵ_F , η_{xx} starts to increase slightly at first. However, increasing μ beyond 0.2 eV (critical point), makes the current fall in the plateau region. Nevertheless, η_{xx} always shows a declining nature when decreasing μ . Therefore, the two approaches mentioned above barely serves our purpose of enhancing the circular photogalvanic effect.

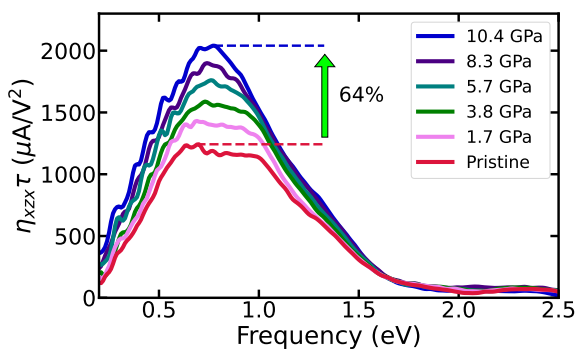


FIG. 5. The multicolored curves represent injection current for different amounts of compressive stress along c -axis. The values increase and the plateau region gradually peaks out at center with increasing stress. The maximum value reaches to $2040 \mu\text{A}/\text{V}^2$ with an increment of 64% at a stress of 10.4 GPa (blue) from the ground state (red).

To account for yet another external influence, we choose strain as the parameter. We apply compressive strain on the unit cell in two different ways: (i) along a -axis and (ii) along c -axis. In the case of (i), we observe a steep decline in the magnitude of η_{xx} . Whereas, applying compressive stress along the c -axis drastically improves the circular photogalvanic effect. We start with the relaxed system in its ground state and gradually decrease the length of c -axis in steps of 1%. The photocurrent profiles for all those strain configurations are depicted in Fig. 5 with the legends implying the stresses corresponding to each step. The maximum value of η_{xx} goes up by 64% from the pristine value at 5% strain corresponding to a stress of 10.4 GPa; which implies a huge current response of $2040 \mu\text{A}/\text{V}^2$. Not only that, the plateau region of the red curve gets sharpened gradually with the application of stress and the peak gets centered in the FWHM region. This leads to a shift of the peak frequency from 0.64 eV to 0.77 eV for a stress of 10.4 GPa.

To understand this effect of strain on CPGE we closely analyze the behavior of electronic structure under strain since the injection current is produced after all due to the interac-

tions between the bands as seen in Eq. (3). In Fig. 6, we plot the band structures (upper row) and the Weyl node-energies (lower row) for various amounts of stress. With increasing stress, the valence and conduction bands shift towards higher energies along the high-symmetry paths $\Gamma - \Sigma$ and $\Gamma - X$ which goes through the bulk Brillouin zone. For instance, the valence band peak along $\Gamma - X$ stays at the Fermi level in absence of stress. However, at higher stresses, the peak goes up significantly from the Fermi level as shown in Figs. 6(a-c). The same behavior is seen for conduction band as well the above-mentioned paths. A different picture is coming out when observing the bands along the path $\Sigma - N - \Sigma_1 - Z$ lying on the outer surface of the Brillouin zone. In this case, the valence and conduction band energies decrease with respect to Fermi level when the stress is increased. This is also easily observed in Figs. 6(a-c) by focusing on the crests and troughs of the bands. In other words, the energy differences between the bands change inhomogeneously throughout the Brillouin zone in presence of stress. Consequently, the integration of the two-band quantities in Eq. (3) throughout the momentum space changes. Another interesting thing to look at is the distribution of Weyl nodes Figs. 6(d-f). The system in its ground state holds 20 pairs of nodes with opposite chirality having energy up to 110 meV . At 5.7 GPa stress, the nodes scatter more in energy scale and remain between -50 to 180 meV . Interestingly, increasing stress beyond this point creates more Weyl points and at a stress of 10.4 GPa , there are 56 nodes in total scattered between -100 and 250 meV . This is due to non-uniform shifting of the bands as we have explained above.

Summary. — We have presented our findings on nonlinear photocurrents in the non-centrosymmetric WSM CeAlSi induced by both linearly and circularly polarized light, using a multi-band approach, derived from the first-principles calculations. Our investigation commenced by analyzing the electronic structure and Berry curvature of CeAlSi. We observed that the material possesses a noncollinear ferromagnetic nature due to the f -electron of Ce atom, thereby breaking the time-reversal symmetry. Moreover, the bands exhibit relatively high magnitudes of Berry curvature. On integration of relevant quantities as described in equations (2) and (3) across 52 bands throughout the Brillouin zone, we were able to determine the shift current responsible for the bulk photovoltaic effect, as well as the injection current driving the circular photogalvanic effect. The results implied that the system exhibits large injection current on irradiation of light compared to the shift current. Notably, the dominant portion of the injection photocurrent is located within the near-infrared (NIR) region of the electromagnetic spectrum. Additionally, we explored various external parameters to modulate the intrinsic photocurrent response. Our findings indicate that a uniaxial compressive strain along the c -axis gives a significant enhancement of the photocurrent. For instance, the application of a stress of 10.4 GPa resulted in a remarkable 64% increase in the injection current compared to the value in the ground state. Upon examining the electronic structure under strain, we found that the non-uniform displacement of the bands in reciprocal space leads to the amplification of the

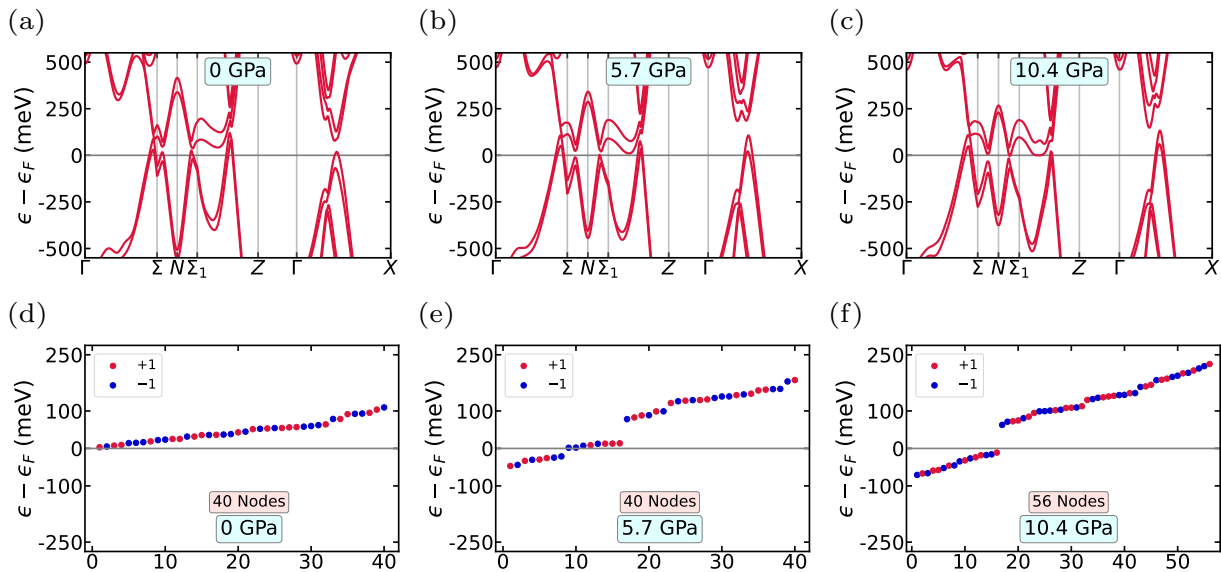


FIG. 6. **Strain-induced band dispersion and Weyl node energies.** (a)-(c) Band structures with SOC for different amounts of uniaxial compressive stress along c -axis. The energy of the valence and conduction bands increases with stress along the paths $\Gamma - \Sigma$ and $\Gamma - X$ which are inside the Brillouin zone. However, the band energies decrease along the path $\Sigma - N - \Sigma_1 - Z$ which lie on the outer surface of the Brillouin zone. (d)-(f) The Weyl nodes are plotted in energy scale and marked their chiralities with distinct colors (*red* and *blue*). The spread in energy increases with increasing stress and goes from 0 – 110 meV to a range between –100 and 180 meV. Moreover, the number of nodes increases to 40 to 56 at a stress of 10.4 GPa.

η -integral. In conclusion, our work suggests that the Weyl semimetal CeAlSi holds great promise for photonic applications as well as a renewable energy source, contributing positively to environmental sustainability.

Acknowledgments. — A.R.K. acknowledges MHRD, Government of India for a research fellowship. We also acknowl-

edge National Supercomputing Mission (NSM) for providing computing resources of “PARAM Shakti” at IIT Kharagpur, which is implemented by C-DAC and supported by the Ministry of Electronics and Information Technology (MeitY) and Department of Science and Technology (DST), Government of India.

-
- [1] N. P. Armitage, E. J. Mele, and A. Vishwanath, Weyl and Dirac semimetals in three-dimensional solids, *Rev. Mod. Phys.* **90**, 015001 (2018).
- [2] A. Bansil, H. Lin, and T. Das, *Colloquium* : Topological band theory, *Rev. Mod. Phys.* **88**, 021004 (2016).
- [3] B. Yan and C. Felser, Topological Materials: Weyl Semimetals, *Annu. Rev. Condens. Matter Phys.* **8**, 337 (2017).
- [4] A. A. Zyuzin, S. Wu, and A. A. Burkov, Weyl semimetal with broken time reversal and inversion symmetries, *Phys. Rev. B* **85**, 165110 (2012).
- [5] D. Xiao, M.-C. Chang, and Q. Niu, Berry phase effects on electronic properties, *Rev. Mod. Phys.* **82**, 1959 (2010).
- [6] K.-Y. Yang, Y.-M. Lu, and Y. Ran, Quantum Hall effects in a Weyl semimetal: Possible application in pyrochlore iridates, *Phys. Rev. B* **84**, 075129 (2011).
- [7] G. Chang, B. J. Wieder, F. Schindler, D. S. Sanchez, I. Belopolski, S.-M. Huang, B. Singh, D. Wu, T.-R. Chang, T. Neupert, S.-Y. Xu, H. Lin, and M. Z. Hasan, Topological quantum properties of chiral crystals, *Nature Mater* **17**, 978 (2018).
- [8] A. Roy Karmakar, S. Nandy, G. P. Das, and K. Saha, Probing mirror anomaly and classes of Dirac semimetals with circular dichroism, *Phys. Rev. Research* **3**, 013230 (2021).
- [9] X. Huang, L. Zhao, Y. Long, P. Wang, D. Chen, Z. Yang, H. Liang, M. Xue, H. Weng, Z. Fang, X. Dai, and G. Chen, Observation of the Chiral-Anomaly-Induced Negative Magnetoresistance in 3D Weyl Semimetal TaAs, *Phys. Rev. X* **5**, 031023 (2015).
- [10] F. Arnold, C. Shekhar, S.-C. Wu, Y. Sun, R. D. Dos Reis, N. Kumar, M. Naumann, M. O. Ajeesh, M. Schmidt, A. G. Grushin, J. H. Bardarson, M. Baenitz, D. Sokolov, H. Borrmann, M. Nicklas, C. Felser, E. Hassinger, and B. Yan, Negative magnetoresistance without well-defined chirality in the Weyl semimetal TaP, *Nat Commun* **7**, 11615 (2016).
- [11] Y. Wang, E. Liu, H. Liu, Y. Pan, L. Zhang, J. Zeng, Y. Fu, M. Wang, K. Xu, Z. Huang, Z. Wang, H.-Z. Lu, D. Xing, B. Wang, X. Wan, and F. Miao, Gate-tunable negative longitudinal magnetoresistance in the predicted type-II Weyl semimetal WTe₂, *Nat Commun* **7**, 13142 (2016).
- [12] A. A. Burkov, Anomalous Hall Effect in Weyl Metals, *Phys. Rev. Lett.* **113**, 187202 (2014).
- [13] J. F. Steiner, A. V. Andreev, and D. A. Pesin, Anomalous Hall Effect in Type-I Weyl Metals, *Phys. Rev. Lett.* **119**, 036601 (2017).
- [14] C. Shekhar, N. Kumar, V. Grinenko, S. Singh, R. Sarkar, H. Luetkens, S.-C. Wu, Y. Zhang, A. C. Komarek, E. Kampert, Y. Skourski, J. Wosnitza, W. Schnelle, A. McCollam, U. Zeitler,

- J. Kübler, B. Yan, H.-H. Klauss, S. S. P. Parkin, and C. Felser, Anomalous Hall effect in Weyl semimetal half-Heusler compounds RPtBi ($\text{R} = \text{Gd}$ and Nd), *Proc. Natl. Acad. Sci. U.S.A.* **115**, 9140 (2018).
- [15] A. Roy Karmakar, S. Nandy, A. Taraphder, and G. P. Das, Giant anomalous thermal Hall effect in tilted type-I magnetic Weyl semimetal $\text{Co}_3\text{Sn}_2\text{S}_2$, *Phys. Rev. B* **106**, 245133 (2022).
- [16] E. V. Gorbar, V. A. Miransky, I. A. Shovkovy, and P. O. Sukhachov, Anomalous thermoelectric phenomena in lattice models of multi-Weyl semimetals, *Phys. Rev. B* **96**, 155138 (2017).
- [17] Y. Ferreira, A. A. Zyuzin, and J. H. Bardarson, Anomalous Nernst and thermal Hall effects in tilted Weyl semimetals, *Phys. Rev. B* **96**, 115202 (2017).
- [18] S. J. Watzman, T. M. McCormick, C. Shekhar, S.-C. Wu, Y. Sun, A. Prakash, C. Felser, N. Trivedi, and J. P. Heremans, Dirac dispersion generates unusually large Nernst effect in Weyl semimetals, *Phys. Rev. B* **97**, 161404 (2018).
- [19] B. Q. Lv, N. Xu, H. M. Weng, J. Z. Ma, P. Richard, X. C. Huang, L. X. Zhao, G. F. Chen, C. E. Matt, F. Bisti, V. N. Strocov, J. Mesot, Z. Fang, X. Dai, T. Qian, M. Shi, and H. Ding, Observation of Weyl nodes in TaAs, *Nature Phys* **11**, 724 (2015).
- [20] S.-Y. Xu, I. Belopolski, D. S. Sanchez, C. Zhang, G. Chang, C. Guo, G. Bian, Z. Yuan, H. Lu, T.-R. Chang, P. P. Shibayev, M. L. Prokopovych, N. Alidoust, H. Zheng, C.-C. Lee, S.-M. Huang, R. Sankar, F. Chou, C.-H. Hsu, H.-T. Jeng, A. Bansil, T. Neupert, V. N. Strocov, H. Lin, S. Jia, and M. Z. Hasan, Experimental discovery of a topological Weyl semimetal state in TaP, *Sci. Adv.* **1**, e1501092 (2015).
- [21] H. Weng, C. Fang, Z. Fang, B. A. Bernevig, and X. Dai, Weyl Semimetal Phase in Noncentrosymmetric Transition-Metal Monophosphides, *Phys. Rev. X* **5**, 011029 (2015).
- [22] U. Dey, S. Nandy, and A. Taraphder, Dynamic chiral magnetic effect and anisotropic natural optical activity of tilted Weyl semimetals, *Sci Rep* **10**, 2699 (2020).
- [23] I. Sodemann and L. Fu, Quantum Nonlinear Hall Effect Induced by Berry Curvature Dipole in Time-Reversal Invariant Materials, *Phys. Rev. Lett.* **115**, 216806 (2015).
- [24] D. Kumar, C.-H. Hsu, R. Sharma, T.-R. Chang, P. Yu, J. Wang, G. Eda, G. Liang, and H. Yang, Room-temperature nonlinear Hall effect and wireless radiofrequency rectification in Weyl semimetal TaIrTe_4 , *Nat. Nanotechnol.* **16**, 421 (2021).
- [25] C. Zeng, S. Nandy, and S. Tewari, Nonlinear transport in Weyl semimetals induced by Berry curvature dipole, *Phys. Rev. B* **103**, 245119 (2021).
- [26] Y.-Y. Lv, J. Xu, S. Han, C. Zhang, Y. Han, J. Zhou, S.-H. Yao, X.-P. Liu, M.-H. Lu, H. Weng, Z. Xie, Y. B. Chen, J. Hu, Y.-F. Chen, and S. Zhu, High-harmonic generation in Weyl semimetal β -WP2 crystals, *Nat Commun* **12**, 6437 (2021).
- [27] B. Lu, S. Sayyad, M. Á. Sánchez-Martínez, K. Manna, C. Felser, A. G. Grushin, and D. H. Torchinsky, Second-harmonic generation in the topological multifold semimetal RhSi , *Phys. Rev. Research* **4**, L022022 (2022).
- [28] Z. Li, Y.-Q. Jin, T. Tohyama, T. Ititaka, J.-X. Zhang, and H. Su, Second harmonic generation in the Weyl semimetal TaAs from a quantum kinetic equation, *Phys. Rev. B* **97**, 085201 (2018).
- [29] G. B. Osterhoudt, L. K. Diebel, M. J. Gray, X. Yang, J. Stanco, X. Huang, B. Shen, N. Ni, P. J. W. Moll, Y. Ran, and K. S. Burch, Colossal mid-infrared bulk photovoltaic effect in a type-I Weyl semimetal, *Nat. Mater.* **18**, 471 (2019).
- [30] J. Ahn, G.-Y. Guo, and N. Nagaosa, Low-Frequency Divergence and Quantum Geometry of the Bulk Photovoltaic Effect in Topological Semimetals, *Phys. Rev. X* **10**, 041041 (2020).
- [31] R. P. Tiwari, B. Birajdar, and R. K. Ghosh, First-principles calculation of shift current bulk photovoltaic effect in two-dimensional α - In_2Se_3 , *Phys. Rev. B* **101**, 235448 (2020).
- [32] F. De Juan, Y. Zhang, T. Morimoto, Y. Sun, J. E. Moore, and A. G. Grushin, Difference frequency generation in topological semimetals, *Phys. Rev. Research* **2**, 012017 (2020).
- [33] F. Flicker, F. De Juan, B. Bradlyn, T. Morimoto, M. G. Vergniory, and A. G. Grushin, Chiral optical response of multifold fermions, *Phys. Rev. B* **98**, 155145 (2018).
- [34] B. Sadhukhan and T. Nag, Electronic structure and unconventional nonlinear response in double Weyl semimetal SrSi_2 , *Phys. Rev. B* **104**, 245122 (2021).
- [35] A. M. Cook, B. M. Fregoso, F. De Juan, S. Coh, and J. E. Moore, Design principles for shift current photovoltaics, *Nat Commun* **8**, 14176 (2017).
- [36] L. Z. Tan, F. Zheng, S. M. Young, F. Wang, S. Liu, and A. M. Rappe, Shift current bulk photovoltaic effect in polar materials—hybrid and oxide perovskites and beyond, *npj Comput Mater* **2**, 16026 (2016).
- [37] V. I. Belinicher and B. I. Sturman, The photogalvanic effect in media lacking a center of symmetry, *Sov. Phys. Usp.* **23**, 199 (1980).
- [38] V. Asnin, A. Bakun, A. Danishevskii, E. Ivchenko, G. Pikus, and A. Rogachev, “Circular” photogalvanic effect in optically active crystals, *Solid State Communications* **30**, 565 (1979).
- [39] G. E. Pikus and E. L. Ivchenko, Photogalvanic effects in non-centrosymmetric semiconductors, in *Narrow Gap Semiconductors Physics and Applications*, Vol. 133, edited by J. Ehlers, K. Hepp, R. Kippenhahn, H. A. Weidenmüller, J. Zittartz, W. Beiglböck, and W. Zawadzki (Springer Berlin Heidelberg, Berlin, Heidelberg, 1980) pp. 388–406.
- [40] H.-Y. Yang, B. Singh, J. Gaudet, B. Lu, C.-Y. Huang, W.-C. Chiu, S.-M. Huang, B. Wang, F. Bahrami, B. Xu, J. Franklin, I. Sochnikov, D. E. Graf, G. Xu, Y. Zhao, C. M. Hoffman, H. Lin, D. H. Torchinsky, C. L. Broholm, A. Bansil, and F. Tafti, Noncollinear ferromagnetic Weyl semimetal with anisotropic anomalous Hall effect, *Phys. Rev. B* **103**, 115143 (2021).
- [41] M. S. Alam, A. Fakhredine, M. Ahmad, P. K. Tanwar, H.-Y. Yang, F. Tafti, G. Cuono, R. Islam, B. Singh, A. Lynnyk, C. Autieri, and M. Matusiak, Sign change of anomalous Hall effect and anomalous Nernst effect in the Weyl semimetal CeAlSi , *Phys. Rev. B* **107**, 085102 (2023).
- [42] M. M. Piva, J. C. Souza, V. Brousseau-Couture, S. Sorn, K. R. Pakuszewski, J. K. John, C. Adriano, M. Côté, P. G. Pagliuso, A. Paramekanti, and M. Nicklas, Topological features in the ferromagnetic Weyl semimetal CeAlSi : Role of domain walls, *Phys. Rev. Research* **5**, 013068 (2023).
- [43] A. P. Sakhya, C.-Y. Huang, G. Dhakal, X.-J. Gao, S. Regmi, B. Wang, W. Wen, R.-H. He, X. Yao, R. Smith, M. Sprague, S. Gao, B. Singh, H. Lin, S.-Y. Xu, F. Tafti, A. Bansil, and M. Neupane, Observation of Fermi arcs and Weyl nodes in a noncentrosymmetric magnetic Weyl semimetal, *Phys. Rev. Materials* **7**, L051202 (2023).
- [44] N. Zhang, X. Ding, F. Zhan, H. Li, H. Li, K. Tang, Y. Qian, S. Pan, X. Xiao, J. Zhang, R. Wang, Z. Xiang, and X. Chen, Temperature-dependent and magnetism-controlled Fermi surface changes in magnetic Weyl semimetals, *Phys. Rev. Research* **5**, L022013 (2023).
- [45] Z. Ni, B. Xu, M.-Á. Sánchez-Martínez, Y. Zhang, K. Manna, C. Bernhard, J. W. F. Venderbos, F. De Juan, C. Felser, A. G. Grushin, and L. Wu, Linear and nonlinear optical responses in the chiral multifold semimetal RhSi , *npj Quantum Mater.* **5**, 96 (2020).
- [46] Z. Ni, K. Wang, Y. Zhang, O. Pozo, B. Xu, X. Han, K. Manna, J. Paglione, C. Felser, A. G. Grushin, F. De Juan, E. J. Mele, and L. Wu, Giant topological longitudinal circular photo-galvanic

- effect in the chiral multifold semimetal CoSi, *Nat Commun* **12**, 154 (2021).
- [47] Y. Zhang, H. Ishizuka, J. Van Den Brink, C. Felser, B. Yan, and N. Nagaosa, Photogalvanic effect in Weyl semimetals from first principles, *Phys. Rev. B* **97**, 241118 (2018).
- [48] F. De Juan, A. G. Grushin, T. Morimoto, and J. E. Moore, Quantized circular photogalvanic effect in Weyl semimetals, *Nat Commun* **8**, 15995 (2017).
- [49] C. Le, Y. Zhang, C. Felser, and Y. Sun, *Ab Initio* study of quantized circular photogalvanic effect in chiral multifold semimetals, *Phys. Rev. B* **102**, 121111 (2020).
- [50] G. Chang, B. Singh, S.-Y. Xu, G. Bian, S.-M. Huang, C.-H. Hsu, I. Belopolski, N. Alidoust, D. S. Sanchez, H. Zheng, H. Lu, X. Zhang, Y. Bian, T.-R. Chang, H.-T. Jeng, A. Bansil, H. Hsu, S. Jia, T. Neupert, H. Lin, and M. Z. Hasan, Magnetic and noncentrosymmetric Weyl fermion semimetals in the R AlGe family of compounds (R = rare earth), *Phys. Rev. B* **97**, 041104 (2018).
- [51] S.-Y. Xu, N. Alidoust, G. Chang, H. Lu, B. Singh, I. Belopolski, D. S. Sanchez, X. Zhang, G. Bian, H. Zheng, M.-A. Husanu, Y. Bian, S.-M. Huang, C.-H. Hsu, T.-R. Chang, H.-T. Jeng, A. Bansil, T. Neupert, V. N. Strocov, H. Lin, S. Jia, and M. Z. Hasan, Discovery of Lorentz-violating type II Weyl fermions in LaAlGe, *Sci. Adv.* **3**, e1603266 (2017).
- [52] G. Kresse and J. Furthmüller, Efficient iterative schemes for *ab initio* total-energy calculations using a plane-wave basis set, *Phys. Rev. B* **54**, 11169 (1996).
- [53] J. P. Perdew, K. Burke, and M. Ernzerhof, Generalized Gradient Approximation Made Simple, *Phys. Rev. Lett.* **77**, 3865 (1996).
- [54] S. L. Dudarev, G. A. Botton, S. Y. Savrasov, C. J. Humphreys, and A. P. Sutton, Electron-energy-loss spectra and the structural stability of nickel oxide: An LSDA+U study, *Phys. Rev. B* **57**, 1505 (1998).
- [55] G. Pizzi, V. Vitale, R. Arita, S. Blügel, F. Freimuth, G. Géranton, M. Gibertini, D. Gresch, C. Johnson, T. Koretsune, J. Ibañez-Azpiroz, H. Lee, J.-M. Lihm, D. Marchand, A. Marrazzo, Y. Mokrousov, J. I. Mustafa, Y. Nohara, Y. Nomura, L. Paulatto, S. Poncé, T. Ponweiser, J. Qiao, F. Thöle, S. S. Tsirkin, M. Wierzbowska, N. Marzari, D. Vanderbilt, I. Souza, A. A. Mostofi, and J. R. Yates, Wannier90 as a community code: New features and applications, *J. Phys.: Condens. Matter* **32**, 165902 (2020).
- [56] D. Gresch, Q. Wu, G. W. Winkler, R. Häuselmann, M. Troyer, and A. A. Soluyanov, Automated construction of symmetrized Wannier-like tight-binding models from *ab initio* calculations, *Phys. Rev. Materials* **2**, 103805 (2018).
- [57] S. S. Tsirkin, High performance Wannier interpolation of Berry curvature and related quantities with WannierBerri code, *npj Comput Mater* **7**, 33 (2021).
- [58] J. E. Sipe and A. I. Shkrebtii, Second-order optical response in semiconductors, *Phys. Rev. B* **61**, 5337 (2000).
- [59] R. W. Boyd, *Nonlinear Optics*, fourth edition ed. (Elsevier, AP Academic Press, London, 2020).